Generation of air lubrication within pyroclastic density currents

Gert Lube [1,7]*, Eric C. P. Breard [2,7], Jim Jones [3], Luke Fullard [4], Josef Dufek [2], Shane J. Cronin [5] and Ting Wang [6]

Pyroclastic density currents are highly dangerous ground-hugging currents from volcanoes that cause >50% of volcanic fatalities globally. These hot mixtures of volcanic particles and gas exhibit remarkable fluidity, which allows them to transport thousands to millions of tonnes of volcanic material across the Earth's surface over tens to hundreds of kilometres, bypassing tortuous flow paths and ignoring rough substrates and flat and upsloping terrain. Their fluidity is attributed to an internal process that counters granular friction. However, it is difficult to measure inside pyroclastic density currents to quantify such a friction-defying mechanism. Here we show, through large-scale experiments and numerical multiphase modelling, that pyroclastic density currents generate their own air lubrication. This forms a near-frictionless basal region. Air lubrication develops under high basal shear when air is locally forced downwards by reversed pressure gradients and displaces particles upward. We show that air lubrication is enhanced through a positive feedback mechanism, explaining how pyroclastic density currents are able to propagate over slopes much shallower than the angle of repose of any natural granular material. This discovery necessitates a re-evaluation of hazard models that aim to predict the velocity, runout and spreading of pyroclastic density currents.

The exceptional mobility of pyroclastic density currents[1-4] remains an enduring open question in volcanic hazard studies[5-10]. This behaviour is surprising because volcanic particles have high static friction of 35–45°, yet they have spectacular flow runouts of 10^1–10^2 km over topography with mean slopes of 8–9°, and even locally upslope (for example, refs. [7,11]). Their high mobility is variously explained by vertical gas escape[12], high gas pore pressure[13], acoustic fluidization[14] and dynamic fragmentation[15], among others[16-18]. The violence of real-world flows has precluded direct measurements, so that none of these processes has been quantitatively validated. Until we can explain the mechanism behind the fluidity of pyroclastic density currents, we cannot adequately forecast hazards for the millions of people at risk[19].

To understand the internal dynamics of pyroclastic density currents, we synthesized them in large-scale experiments using the Pyroclastic flow Eruption Large-scale Experiment (PELE) eruption simulator facility[20,21]. Here, experimental pyroclastic density currents are generated by the controlled gravitational collapse of an aerated suspension of natural volcanic particles from a heated hopper into an instrumented flume[20]. The mixture falls into a 12-m-long and 0.5-m-wide inclined channel (variable between 6 and 18°, with a basal friction angle of 36.5° and basal roughness of ~0.2 mm) before spreading out onto a flat concrete pad (with a basal friction angle of 37.5°).

Flows are measured using high-speed video through a glass wall of the flume. High-precision load cells and piezoresistive pressure sensors in the channel base measure the flowing mass and static gas pore pressure (total pressure minus dynamic pressure, relative to the atmosphere).

For each experiment, we used between 1,000 and 1,300 kg of natural volcanic particles from the AD232 Taupo eruption[22]

(static internal friction angle of 39°; Supplementary Fig. 1) at temperatures between 15 and 130 °C. A detailed description of the experimental conditions and scaling similitude to real-world flows is available in ref. [20] and also summarized in the Methods and Supplementary Tables 1–3. On impact with the flume, the mixture simulates a collapsing volcanic eruption column and contains ~7.5 vol.% solids. Once flowing down the flume, the suspension rapidly segregates into a basal underflow (up to 0.8 m thick) and an over-riding ash cloud (2.0–4.5 m high). The underflow contains 40 vol.% particles, including the bulk of the coarse material, while the over-riding cloud contains only 7×10^{-3} vol.% (Figs. 1b and 2a and Supplementary Video 1). The ash cloud runs out to 35 m, while the underflow reaches 18.7–26.5 m, depending on the initial fall height (3.0–5.4 m) and channel inclination. Deposits from these experiments are 0.02–0.40 m thick.

Characterizing synthetic pyroclastic density currents

The apparent friction coefficients of the experimental underflows, μ_{app}, range between 0.2 and 0.31, as estimated from the ratio of the drop to the runout length. These are only 25–39% of the static friction coefficient of the particles ($\mu_{ash} = 0.8$), and overlap with values for natural flow deposits[23].

To visualize internal flow dynamics, we compute the time- and height-variant particle solids concentration of the underflow at a single location (Fig. 2b). This is done by numerically back-calculating the space- and time-variant expansion and contraction of the underflow from the end of the experiment, t_f, where the underflow is deposited and has a height-invariant solids volume fraction, backwards in time until underflow arrival at t_0 (see Methods for details). During flow, and up to the onset of deposition, the particle concentration varies strongly with height, with a general trend of the

Fig. 1 | Synthesizing pyroclastic density currents in large-scale experiments. a, Oblique view of an advancing experimental pyroclastic density current at the eruption simulator PELE along the concrete pad at the end of the flume. **b**, Series of images of the lower 0.95 m of the flow passing an observation point at 3.2 m. Arrows highlight the boundary between the concentrated basal underflow and the dilute, turbulent over-riding ash cloud.

concentration decreasing downwards in the underflow. Furthermore, a 20–40-mm-thick basal layer develops with particle concentrations around half those of the over-riding zone (19–24 vol.% versus 35–54 vol.%) (Fig. 2b). Gas escaping from this basal zone produces elutriation pipes that rise upward immediately before the flow arrests (Supplementary Fig. 2 and Supplementary Video 2).

Gas escape implied that an overpressure had developed in the experimental flows. The total basal pore pressure, P_{total}, can be defined as:

$$P_{total} = P_{static} + P_{dynamic} = P_{static} + 0.5\rho_{base}v_{base}^2 \quad (1)$$

where P_{static} is the measured static pressure, and ρ_{base} and v_{base} are the flow density and velocity at the base. Fig. 2c shows that the total basal pore pressure is positive (~0.1–1.1 kPa) during the presence of the basal low particle concentration zone. During runout, the pore pressure gradually decays within the underflow (Fig. 2c). The degree of bed support that the underflow provides, N, is given by:

$$N = \frac{P_{total}}{g\int_0^{h_m}\rho(h)\,dh} \quad (2)$$

where g is the gravitational constant, ρ is the height-variant density, and h and h_m are the height- and time-variant maximum height of the underflow.

An energy budget illustrates the unaccounted for energy associated with friction, which can be used to establish an effective friction coefficient. For a small distance of downslope travel, s, the energy balance is given by:

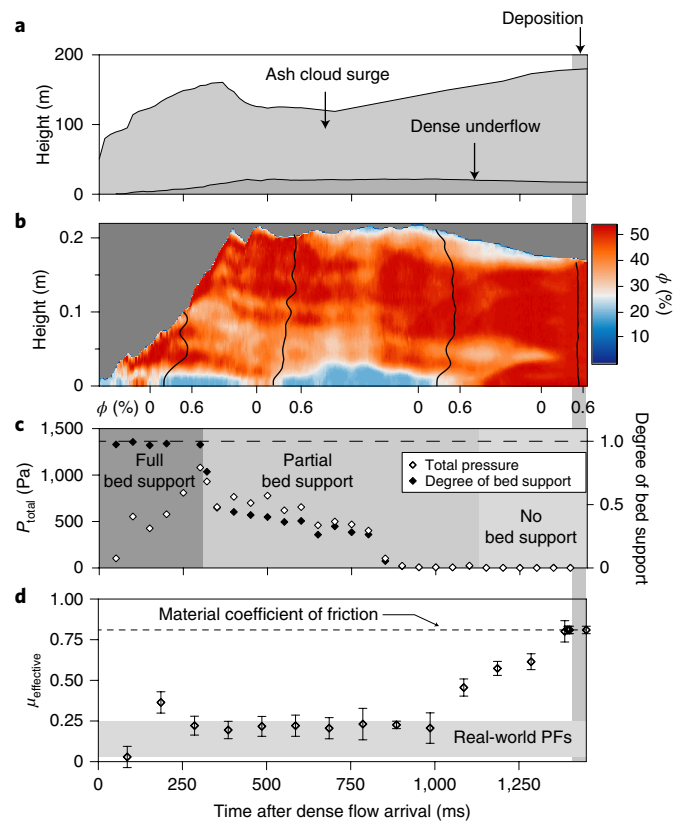$$E_{pot\_1} + E_{kin\_1} = E_{pot\_2} + E_{kin\_2} + E_{friction} \quad (3)$$

Fig. 2 | Time-variant flow properties at 5.6 m. a, Heights of the underflow and ash cloud. **b**, Contour plot of particle solids concentration (ϕ) of the passing underflow against time after dense flow arrival; vertical profiles of ϕ (shown in the range 0–0.6%) at four different times; a 20–40-mm-thick region with a strongly reduced solids concentration occurs below an upper concentrated region. **c**, Basal total gas pore pressure, P_{total} (white diamonds) and degree of bed support (black diamonds). **d**, Effective depth-averaged friction coefficient. Error bars account for local fluctuations of velocity fields over 0.5 ms. The occurrence of a low-concentration basal zone coincides with ultra-low friction values (the grey box indicates the range of apparent friction coefficients of real-world pyroclastic flows (PFs)).

where E_{pot} and E_{kin} are potential and kinetic energy values, respectively. Over distances of a few centimetres in the scale of our experiment, mass and volume are conserved, and variations in kinetic and potential energy can be calculated from the measured flow height, mass and depth-averaged velocity. The time-variant effective coefficient of friction, $\mu_{effective}$, is given by:

$$\mu_{effective} = \frac{E_{friction}}{F_N s} = \frac{0.5(v_1^2 - v_2^2)}{gs\cos\alpha} + \tan\alpha \quad (4)$$

where F_N is the local normal force and α is the slope of the substrate. The subscripts refer to conditions across an increment of travel distance. This relation describes the effective mobility that may be associated with a range of momentum redistribution mechanisms operating locally, and the variability of the material static friction coefficient. Using this approach, the depth-averaged friction coefficients reach as low as 0.19 when the low-particle concentration zone is present. This is only 23% of the static coefficient of friction (Fig. 2d) and corresponds to the low values of apparent friction attained by natural flows. Friction increases again during final deceleration after ~90% of the flow has passed the observer location.

The phenomenon of a low-concentration basal zone was recently observed in smaller bench top-scale experiments and discrete
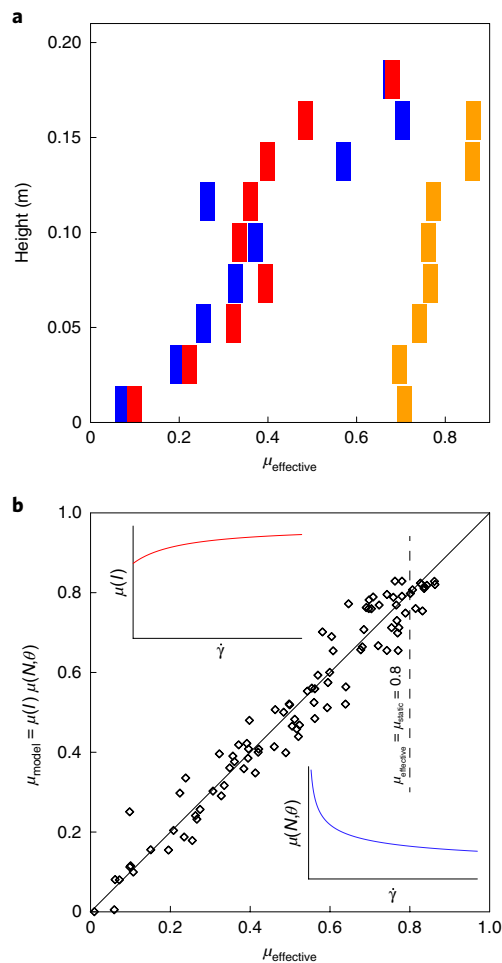
Fig. 3 | Height-variant friction and a test of the effective friction coefficient law. a, Effective friction coefficients for 20-mm-thick slope-normal control volumes at 380 ms (blue), 690 ms (red) and 1,290 ms (orange). **b**, Modelled data of the effective friction coefficients (equation (5)) against measured control volume-averaged effective friction coefficients obtained at 100 ms intervals. Insets, opposite trends of functions $\mu(I)$ (top left) and $\mu(\theta,N)$ (bottom right), the product of which is $\mu_{effective}$ (equation (5)), against the shear rate $\dot{\gamma}$.

(gas-free) particle simulations of dry granular flows[24,25]. These are especially observed under steep slopes close to the material static angle of friction with a bumpy base. Under such conditions, particles become highly agitated and there is a shear-induced increase in the collision rate and particle dispersion. However, in contrast with our results, these conditions, where the role of interstitial gas is ignored, also increase the apparent viscosity, as illustrated by the $\mu(I)$ friction law, where I is the inertia number[26,27]. Pyroclastic density currents[28] and our work both show a strong reduction in friction.

Rheological description of the critical basal region

The above results pose an important question: how does low friction evolve in these volcanic particle–air mixture flows? To study this, we subdivided the underflow vertically into control volumes of 0.02 m thicknesses to obtain (control volume-averaged) effective friction coefficients at intervals of 100 ms (equations (3) and (4)). This approach reveals that the effective friction varies strongly with height (Fig. 3a), with ultra-low values ranging from 0.05–0.21, occurring in the lowermost basal control volume, above which
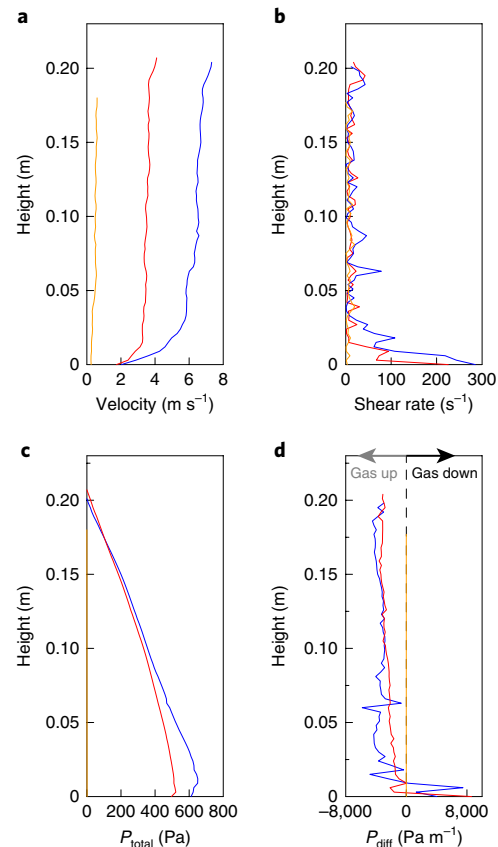

Fig. 4 | Origin and potential for air lubrication in experimental pyroclastic density currents. Height-variant data are presented for three different times at the static observer location at 5.6 m: 380 ms (blue), 690 ms (red) and 1,290 ms (orange). **a**, Slope-normal velocity profiles of the underflow. **b**, Slope-normal shear rate profiles of the underflow. **c**, Vertical profiles of the total pressure P_{total}, as estimated from equation (1) using measurements of flow velocity, density and basal static pressure, and assuming that the degree of bed support (equation (2)) is height invariant. **d**, Profiles of the pressure gradient P_{diff}, being the vertical gradient of P_{total}, where $P_{total} > 0$ implies local downward gas advection.

$\mu_{effective}$ progressively increases. Friction in the mid-flow region is 0.3–0.4, rising to 0.6–0.7 in the uppermost part of the flow. During flow arrest, effective friction coefficients return to the static material friction values as bed support ceases and the low-concentration basal region disappears.

The decrease in friction in the basal control volumes analysed corresponds to a low particle concentration (Fig. 2b), high shear rate (Fig. 4b) and positive pressure gradient (Fig. 4c,d). In these zones, the flow glides along the base at slip velocities up to 5 m s⁻¹ (Fig. 4a and Supplementary Video 2). This produces a lower (~20–50-mm-thick) zone of very high shear (~40–300 s⁻¹) overlain by a region with low shear (5–26 s⁻¹) (Fig. 4b). The basal slip remains until flow velocities decrease below 0.01 m s⁻¹. A local positive pressure arises in the basal region because it is dominated by the shear-induced differential velocity (equation (1)).

We suggest that the $\mu(I)$ rheology of dry granular flows[26,27] can be extended to account for local and transient changes induced in the basal plane. Here, the slip shear stress τ is a function of the normal stress σ_N, where the effective friction coefficient can be described using the friction law adapted to the dimensionless concentration θ/θ_m. We add an effective fluidization parameter, $1 - N$, where N is the fractional bed support (equation (2)):
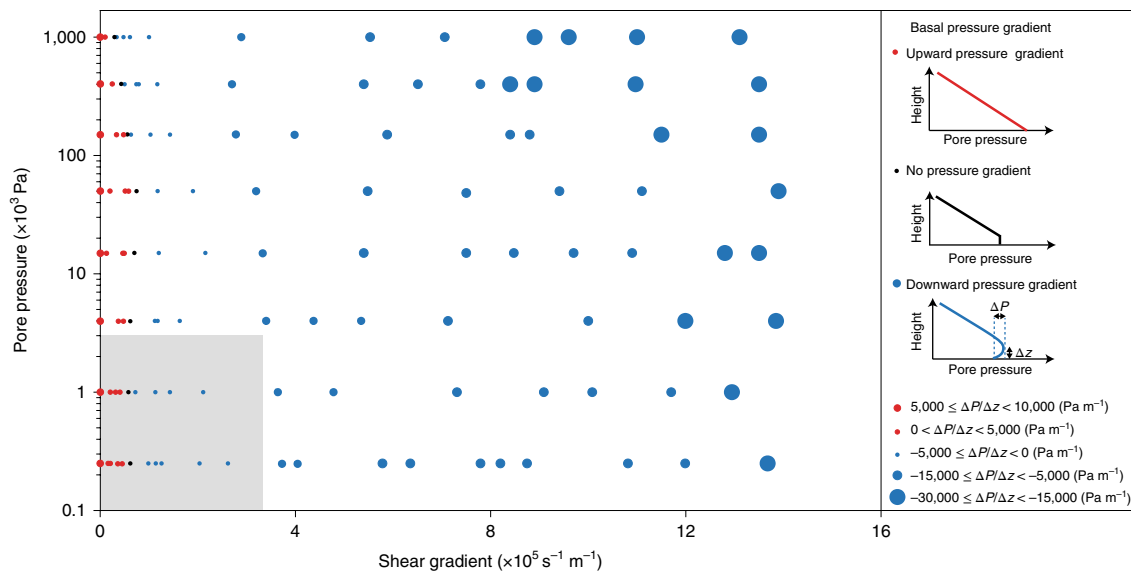
Fig. 5 | Occurrence of basal air lubrication in pyroclastic density currents. Results of 134 Lagrangian–Eulerian multiphase simulations for natural ranges of basal shear gradients (0.001×10^5 to $14\,s^{-1}\,m^{-1}$) and pore pressures (250–1,000,000 Pa) (the shaded rectangle shows the experimental range). Three regimes of basal pressure gradient are delineated: (1) upward pressure gradients (red dots), driving upward gas advection; (2) no pressure gradient (black dots); and (3) downward pressure gradient (blue dots), forcing downward gas pressure advection and air lubrication. The dot sizes distinguish five ranges of pressure gradient $\Delta P/\Delta z$, where ΔP is the difference between the maximum bed pore pressure and the pore pressure in the lowermost computational cell, across height Δz.

$$
\begin{aligned}
\tau &= [\mu_{\text{effective}}]\,\sigma_N = [(\mu(I))\,(\mu(\theta, N))]\,\sigma_N \\
&= \left[\left((\mu(I))\left(\left(\frac{\theta}{\theta_m}\right)^n (1-N)\right)\right)\right]\rho g h
\end{aligned}
\tag{5}
$$

The terms θ and θ_m are the local and close-packed concentrations, and n is a constant. In this phenomenological expression, the model product $\mu(I)\,\mu(\theta, N)$ can be seen as equivalent to the effective friction coefficient. The measured and modelled effective friction coefficients $\mu_{\text{effective}}$ and μ_{model} compare well when $n = {\sim}2$ (Fig. 3b).

The two terms of the model show contrasting effects of the shear rate on energy dissipation. The $\mu(I)$ term increases with rising shear rate, while $\mu(N, \theta)$ decreases (insets Fig. 3b). Our measured effective friction coefficients are below the material static friction coefficient, so the term $\mu(N, \theta)$ must dominate energy dissipation. This implies that it is not granular dilatancy[29] that controls transient changes in the particle concentration of our experimental mixture.

Air-lubrication mechanism

Here, we propose a pressure-driven air-lubrication mechanism for our experimental pyroclastic flows. In particle-gas flows, gas advection is driven by the pressure gradient, which leads to dynamic changes in particle concentration and gas pore pressure. In fluidized beds, the pressure gradient is always upward, forcing upward advection of air until complete defluidization. Pyroclastic density currents include horizontal shear that disrupts this process. In these, downslope acceleration is restricted by interparticle and basal friction generating variable velocity and shear with height (for example, Fig. 4a,b). Conservation of mass, momentum and energy dictates that local acceleration of the gas phase due to shear gradients will generate static pressure gradients (or stored energy density). For our experimental flows, the local pressure gradient in the basal region becomes positive up to several kilopascals per metre (Fig. 4d). In a two-phase mixture, this results in differential motion of gas and particles. Gas has low inertia and thus moves along the pressure gradient into the low-pressure basal zone. This dilutes the local particle

concentration (see Fig. 2b), so that the basal region of the underflow accumulates gas, which consequently reduces resistance to shearing (Fig. 3a). This friction-reduction process is reinforced by simultaneous shear-induced migration of particles into low-shear regions[30].

Flows lubricated by air in this way show lower deceleration, which perpetuates high basal shear gradients. This in turn sustains a downward pressure gradient and gas supply into the basal zone. Furthermore, it delays the upward defluidization of gas from the entire flow.

Air lubrication in real-world flows

We consider that basal air lubrication regularly occurs in natural pyroclastic flows. Using a discrete element model (DEM) coupled to a Eulerian gas phase (Multiphase Flow with Interface eXchange) (MFIX-DEM)[31–33], we simulated coupled particle-gas[34] flows for a wide range of natural flow thicknesses, velocities and degrees of bed support, and at a natural temperature of 400 °C. Models were focused on the basal region of the flows by simulating a 0.2-m-high domain, wherein a set gas pore pressure was imposed at the top boundary as a hydrostatic pressure. In this way, simulations were performed for underflows of up to 100 m high. A simulation with 10 kPa pressure corresponds to a 1-m-thick flow with full bed support, or a 10-m-thick flow with 10% bed support. Simulations were carried out with overpressure between 0.25 and 1,000 kPa (the range of pumice pyroclastic density currents and block-and-ash flows up to 100 m thick) and vertical shear rate gradients from 4×10^2 to $1.5 \times 10^6\,m^{-1}\,s^{-1}$. Other technical details of the numerical simulations are reported in the Methods.

The simulations show two behaviours (Fig. 5). At very low shear gradients, flows show an upward pressure gradient and no air lubrication. As shear gradients rise, flows exhibit a basal downward pressure gradient, leading to basal dilution, reduced friction and air lubrication. Between these two regimes is a narrow range of shear rate gradients of $20{,}000–40{,}000\,m^{-1}\,s^{-1}$, at which no pressure gradient occurs, and which only weakly depends on the absolute value of pore pressure (or underflow thickness). All three behaviours were seen in the physical experiments under velocities of $2–6\,m\,s^{-1}$.

The numerical simulations show that downward percolation of air through a shearing flow is highly efficient (within milliseconds) and several orders of magnitude faster than gravity compaction. This implies that basal air lubrication is probable in natural pyroclastic density currents[35,36] over most of their runout distance.

Air lubrication is a variant of the pore-pressure feedbacks described in water-particle flows[37,38]. However, pyroclastic density currents introduce additional dynamics because, unlike water-particle flows, they contain low-density compressible gases that respond quickly to local changes in pore pressure. Gas advection far outpaces gravity compaction, whereas in water systems, they occur over similar time scales. Dilution of the particle concentration in a thin basal boundary layer produced fewer interparticle collisions, which is a consequence of the greater effect of lower particle concentration than high shear rate on the overall interparticle collision rate. Thus, less effective friction results, further increasing the shear and the pressure gradient for gas advection. This feedback continues until other factors become important—probably a changing resistance of the overburden to gas advection—due to the local increase in the solids volume fraction and/or the formation of gas bubbles, which later become elutriation pipes. Over longer time scales, and unlike water-particle flows[39], the dynamics of pore-pressure dissipation will become strongly influenced by gravity compaction[40].

Discovery of the air-lubrication mechanism opens a new perspective on the known extreme runout potential of these lethal currents. With eyes on global hazard mitigation strategies, the demonstrated self-generated reduction of basal effective friction in these flows provides a compelling explanation for the ability of early depth-averaged models[28,41,42] to achieve similarity with observed natural flows. In these models, empirically imposed very low basal friction was able to capture essential aspects of the flow runout and frontal velocity dynamics. The efficiency of air lubrication in our comparably slow experimental flows suggests that it must be present in other types of long runout mass flows, including snow avalanches and fast-flowing landslides.

Online content

Any methods, additional references, Nature Research reporting summaries, source data, statements of data availability and associated accession codes are available at https://doi.org/10.1038/s41561-019-0338-2.

References

1. Valentine, G. A. Damage to structures by pyroclastic flows and surges, inferred from nuclear weapons effects. *J. Volcanol. Geotherm. Res.* **87**, 117–140 (1998).
2. Branney, M. & Kokelaar, P. *Pyroclastic Density Currents and the Sedimentation of Ignimbrites* Geological Society Memoir No. 27 (Geological Society, London, 2002).
3. Sulpizio, R., Dellino, P., Doronzo, D. M. & Sarocchi, D. Pyroclastic density currents: state of the art and perspectives. *J. Volcanol. Geotherm. Res.* **283**, 36–65 (2014).
4. Dufek, J., Esposti Ongaro, T. & Roche, O. in *The Encyclopedia of Volcanoes* 2nd edn (ed. Sigurdsson, H.) 617–629 (Academic Press, 2015).
5. Wilson, C. J. N. The role of fluidization in the emplacement of pyroclastic flows: an experimental approach. *J. Volcanol. Geotherm. Res.* **8**, 231–249 (1980).
6. Wilson, C. J. N. The Taupo eruption, New Zealand. II. The Taupo ignimbrite. *Phil. Trans. A Math. Phys. Eng. Sci.* **314**, 229–310 (1985).
7. Roche, O., Buesch, D. C. & Valentine, G. A. Slow-moving and far-travelled dense pyroclastic flows during the Peach Spring super-eruption. *Nat. Commun.* **7**, 10890 (2016).
8. Francis, P. W. & Baker, M. C. W. Mobility of pyroclastic flows. *Nature* **270**, 164–165 (1977).
9. Girolami, L., Roche, O., Druitt, T. H. & Corpetti, T. Particle velocity fields and depositional processes in laboratory ash flows, with implications for the sedimentation of dense pyroclastic flows. *Bull. Volcanol.* **72**, 747–759 (2010).
10. Druitt, T. H., Bruni, G., Lettieri, P. & Yates, J. G. The fluidization behaviour of ignimbrite at high temperature and with mechanical agitation. *Geophys. Res. Lett.* **31**, L02604 (2004).
11. Cas, R. A. F. et al. The flow dynamics of an extremely large volume pyroclastic flow, the 2.08-Ma Cerro Galan Ignimbrite, NW Argentina, and comparison with other flow types. *Bull. Volcanol.* **73**, 1583–1609 (2011).
12. Sparks, R. S. J. Grain size variations in ignimbrites and implications for the transport of pyroclastic flows. *Sedimentology* **23**, 147–188 (1976).
13. Roche, O. Depositional processes and gas pore pressure in pyroclastic flows: an experimental perspective. *Bull. Volcanol.* **74**, 1807–1820 (2012).
14. Melosh, H. J. Acoustic fluidization: a new geologic process? *J. Geophys. Res. Solid Earth* **84**, 7513–7520 (1979).
15. Dufek, J. & Manga, M. In situ production of ash in pyroclastic flows. *J. Geophys. Res.* **113**, B09207 (2008).
16. Shreve, R. L. The Blackhawk landslide. *Geol. Soc. Am. Spec. Pap.* **108**, 1–47 (1968).
17. Lucas, A., Mangeney, A. & Ampuero, J. P. Frictional velocity-weakening in landslides on Earth and on other planetary bodies. *Nat. Commun.* **5**, 3417 (2014).
18. Lube, G., Huppert, H. E., Sparks, R. S. J. & Hallworth, M. A. Axisymmetric collapses of granular columns. *J. Fluid Mech.* **508**, 175–199 (2004).
19. National Academies of Sciences, Engineering, and Medicine *Volcanic Eruptions and Their Repose, Unrest, Precursors, and Timing* (National Academies Press, 2017); https://doi.org/10.17226/24650
20. Lube, G., Breard, E. C. P., Cronin, S. J. & Jones, J. Synthesizing large-scale pyroclastic flows: experimental design, scaling, and first results from PELE. *J. Geophys. Res. Solid Earth* **120**, 1487–1502 (2015).
21. Breard, E. C. P. et al. Coupling of turbulent and non-turbulent flow regimes within pyroclastic density currents. *Nat. Geosci.* **9**, 767–771 (2016).
22. Hogg, A., Lowe, D. J., Palmer, J., Boswijk, G. & Ramsey, C. B. Revised calendar date for the Taupo eruption derived by ^{14}C wiggle-matching using a New Zealand kauri ^{14}C calibration data set. *Holocene* **22**, 439–449 (2012).
23. Hayashi, J. N. & Self, S. A comparison of pyroclastic flow and debris avalanche mobility. *J. Geophys. Res.* **97**, 9063–9071 (1992).
24. Taberlet, N., Richard, P., Jenkins, J. T. & Delannay, R. Density inversion in rapid granular flows: the supported regime. *Eur. Phys. J. E* **22**, 17–24 (2007).
25. Brodu, N., Delannay, R., Valance, A. & Richard, P. New patterns in high-speed granular flows. *J. Fluid Mech.* **769**, 218–228 (2015).
26. Jop, P., Forterre, Y. & Pouliquen, O. A constitutive law for dense granular flows. *Nature* **441**, 727–730 (2006).
27. Da Cruz, F., Emam, S., Prochnow, M., Roux, J.-N. & Chevoir, F. Rheophysics of dense granular materials: discrete simulation of plane shear flows. *Phys. Rev. E* **72**, 021309 (2005).
28. Kelfoun, K. Suitability of simple rheological laws for the numerical simulation of dense pyroclastic flows and long-runout volcanic avalanches. *J. Geophys. Res.* **116**, B08209 (2011).
29. Forterre, Y. & Pouliquen, O. Flows of dense granular media. *Annu. Rev. Fluid Mech.* **40**, 1–24 (2008).
30. Leighton, D. & Acrivos, A. The shear-induced migration of particles in concentrated suspensions. *J. Fluid Mech.* **181**, 415–439 (2006).
31. Garg, R., Galvin, J., Li, T. & Pannala, S. Open-source MFIX-DEM software for gas–solids flows: part I—verification studies. *Powder Technol.* **220**, 122–137 (2012).
32. Li, T., Garg, R., Galvin, J. & Pannala, S. Open-source MFIX-DEM software for gas–solids flows: part II—validation studies. *Powder Technol.* **220**, 138–150 (2012).
33. Syamlal, M., Rogers, W. & O'Brien, T. J. *MFIX Documentation: Theory Guide* (US Department of Energy, 1993).
34. Gidaspow, D. *Multiphase Flow and Fluidization: Continuum and Kinetic Theory Description* (Academic Press, Cambridge, 1994).
35. Druitt, T. H. et al. Small-volume, highly mobile pyroclastic flows formed by rapid sedimentation from pyroclastic surges at Soufriere Hills Volcano, Montserrat: an important volcanic hazard. *Mem. Geol. Soc. Lond.* **21**, 263–279 (2002).
36. Lube, G., Cronin, S. J., Thouret, J.-C. & Surono. Kinematic characteristics of pyroclastic density currents at Merapi and controls on their avulsion from natural and engineered channels. *Geol. Soc. Am. Bull.* **123**, 1127–1140 (2011).
37. Iverson, R. M. Regulation of landslide motion by dilatancy and pore pressure feedback. *J. Geophys. Res. Earth Surf.* **110**, F02015 (2005).
38. Iverson, R. M. & Lahusen, R. G. Dynamic pore-pressure fluctuations in rapidly shearing granular materials. *Science* **246**, 796–799 (1989).
39. Iverson, R. M. et al. Positive feedback and momentum growth during debris-flow entrainment of wet bed sediment. *Nat. Geosci.* **4**, 116–121 (2011).
40. Breard, E. C. P., Dufek, J. & Lube, G. Enhanced mobility in concentrated pyroclastic density currents: an examination of a self-fluidization mechanism. *Geophys. Res. Lett.* **45**, 654–664 (2018).
41. Sheridan, M. F. Emplacement of pyroclastic flows: a review. *Geol. Soc. Am. Spec. Pap.* **180**, 125–136 (1979).

42. Charbonnier, S. J. & Gertisser, R. Numerical simulations of block-and-ash flows using the Titan2D flow model; examples from the 2006 eruption of Merapi Volcano, Java, Indonesia. *Bull. Volcanol.* **71**, 953–959 (2009).

Author contributions

G.L. designed the experiments and wrote the first draft of the manuscript, which was then revised by all the authors. G.L. and E.C.P.B. conducted and analysed the experiments, and interpreted the data together with J.J. L.F. and T.W. conducted the advection analysis. E.C.P.B. and J.D. conducted the numerical simulations. G.L., S.J.C. and J.J. developed the PELE facility.

Competing interests

The authors declare no competing interests.

Additional information

Supplementary information is available for this paper at https://doi.org/10.1038/s41561-019-0338-2.

Reprints and permissions information is available at www.nature.com/reprints.

Correspondence and requests for materials should be addressed to G.L.

Publisher's note: Springer Nature remains neutral with regard to jurisdictional claims in published maps and institutional affiliations.

Methods

Large-scale experiments. The eruption simulator PELE (fully described in ref. [20]) is a unique test facility where we can synthesize, view and measure inside the highly dangerous interior of pyroclastic density currents. Experimental currents of up to 6 tonnes of natural volcanic material and gas reach velocities of $7–32\,m\,s^{-1}$, flow thicknesses of 2.0–4.5 m and runouts of > 35 m (ref. [20]). PELE synthesizes experimental pyroclastic density currents by the controlled gravitational collapse of variably diluted suspensions of pyroclastic particles and gas from an elevated hopper onto an instrumented runout section. PELE is operated indoors, inside a 16-m-high, 25-m-long and 18-m-wide disused boiler house. The apparatus contains four main structural components as follows. (1) A 13-m-high tower that lifts a 4.2 m³ hopper to the desired discharge height. This includes an internal hopper heating unit to bring the pyroclastic material to target temperatures of up to 400 °C. It is mounted on four load cells to capture the time-variant mass discharge. (2) A ≤9-m-high column through which the air-particle mixtures accelerate under gravity. (3) A 12-m-long multi-instrumented chute that is variably adjustable to slope angles between 5 and 25° and with 0.6–1.8-m-high sides of temperature-resistant glass. (4) A 25-m-long flat instrumented outflow section that extends outside the building. The physical characteristics of the gas-particle suspensions before impact (velocity, mass flux, volume flux, particle concentration and temperature), solids components (grain-size distribution and density) and boundary conditions (substrate roughness, slope and channel width) can be controlled to generate a wide range of reproducible natural conditions[20]. The input and boundary conditions for the reported experiments are given in Supplementary Table 3.

The use of volcanic material and air in our experiments ensured natural stress coupling between the solid and fluid phases. The volcanic starting material, involving particle sizes from 2 μm to 64 mm, constituted a blend of two standardized ignimbrite deposits F1 and F2 from the AD232 Taupo eruption[22]. The first component (F1) was a proximal medium-ash-dominated ignimbrite deposit with a unimodal grain-size distribution, a median diameter of 366 μm and 4.5 wt.% of extremely fine ash (<63 μm). The second component (F2) was a fine ash-rich facies from the base of the proximal Taupo ignimbrite, showing a polymodal distribution, a median diameter of 103 μm and 36.5 wt.% extremely fine ash. The experiments reported here used a material blend with F1 = 67 wt.% and F2 = 33 wt.% (see the grain-size distribution in Supplementary Fig. 1), yielding a mixture with 15% by weight of particles smaller than 63 μm.

The resulting pyroclastic density current analogues are fully turbulent, with Reynolds numbers up to 10⁶ and, in proximal regions, even in the lower range of 10⁷. Dimensionless products quantifying the scaling similitude of natural and experimental currents for both the bulk flow and the dense underflow are shown in Supplementary Tables 1 and 2. Further details of the experimental protocol, properties of the volcanic material and measurement techniques are described elsewhere[20], but some measurements and analytical methods specific to the results presented here are detailed below.

Sensors and analytical methods. Two fast cameras (60–120 frames per second) and two normal-speed cameras (24–30 frames per second), positioned at different distances, viewing angles and directions, recorded the downstream evolution of the experimental pyroclastic density currents. At a runout distance of 5.6 m, a digital high-speed camera (nac HotShot at 2,000 frames per second) recorded the flow passage of the lower 0.4 m of the flow, capturing the entire dense underflow and the lower part of the ash cloud. The high-temperature glass walls of the channel were illuminated by a 5,500 W light array, which allowed for a detailed analysis of the gas-particle transport and sedimentation processes with particle image velocimetry (PIV; using the algorithm PIVlab). Two-dimensional velocity fields were obtained with PIV from the high-speed footage at 0.5 ms time intervals.

At a runout distance of 5.6 m, a high-precision s-beam load cell (AML-DBBSM), manufactured for measurements on inclined surfaces, and a piezoresistive pressure transducer (MS ICS 154N) were mounted into the flow base and calibrated, to capture time-series data of the flow mass and basal static pressure. The load cell was connected to a circular steel plate of 0.1 m diameter, whose upper surface was installed flush with the channel while a ring of plastic foil (glued over the base plate/channel base boundary) produced an air- and particle-proof seal. The top of the pressure transducer was shielded from particle contact by a 1.5-mm-thick air gap and a 1-mm-thick sandwich of crossed layers of nylon and steel sieves, the latter of which was installed flush with the channel base.

The mass fraction of the material transported in the dilute ash cloud relative to the whole flow mass is negligibly small (0.48 wt.%). This allows for calculation of the depth-averaged particle volumetric concentration of the underflow $\tilde{\phi}$, as follows:

$$\tilde{\phi} = \frac{M_{flow}}{A H_U \rho_p} \tag{6}$$

where A is the area of the load cell, M_{flow} is the flow mass (the sum of the weight recorded by the load cell and the basal pressure, converted to a load) passing at an observer location, H_U is the time-variant thickness of the underflow measured in high-speed videos, and ρ_p is the average particle density.

Time-variant values of the (depth-averaged) velocity, flow height H_U and (depth-averaged) solids concentration $\tilde{\phi}$ at 5.6 m were used to compute the time-variant mass flux and, subsequently through integration, the total mass M_{t_int} that passed this distance. M_{t_int} is only 2.3% smaller than the independently measured value of the mass of deposit M_{t_dep} emplaced downstream of 5.6 m. This shows that the two-dimensional velocity fields obtained at the glass side walls via PIV are representative for the underflow dynamics across the channel width, and that components of velocity perpendicular to the glass side walls are negligible.

PIV results in two-dimensional velocity fields of the underflow resolved into 370 × 495 cells. The height- and time-variant particle solids concentrations of the underflow presented in Fig. 2b were computed numerically by solving for each cell the conservative form of the advection equation using the two-dimensional velocity fields obtained through PIV:

$$\phi_t + (u\phi)_x + (v\phi)_y = 0 \tag{7}$$

where ϕ is the solids fraction, u and v are the horizontal and vertical components of velocity, respectively, which are known (measured by PIV), and the subscripts refer to the partial derivatives. For each time step of 0.5 ms, equation (7) is solved for ϕ, the depth-averaged value of which, $\tilde{\phi}$, is the experimentally determined.

Note that this equation is derived from an expression of the conservation of solid particle mass. Since the solid-phase particle density is assumed to be constant, it can be removed from the t, x and y derivatives and eliminated, yielding the conservative advection equation for ϕ. The advection partial differential equation is a hyperbolic equation, which permits us to solve it in either the forwards or backwards time directions and for it to still be a mathematically well-posed problem. Equation (7) is solved from the end of the experiment backwards, because at this time, t_f, the deposit of the underflow is static; the concentration is height invariant and corresponds to the experimentally determined depth-averaged concentration $\tilde{\phi}(t_f)$. Using this value as an initial condition, $\tilde{\phi}(t_f) = \phi_0$, we make a mathematical transformation to the advection equation:

$$T = t - t_f \tag{8}$$

so that $\phi = \phi_0$ at transformed time $T = 0$, and we solve the partial differential equation backwards in real time until $T = t_f$.

A first-order finite-volume upwind method was used to discretize the governing equation, such that the flux was evaluated at the boundary of each cell. The boundary conditions used in the analysis were upper, lower and side boundaries. For the upper boundary, $\phi = 0$, while for the lower boundary, a reflective boundary was used so that no mass could leave the grid from below. This was implemented by the use of a ghost cell with $\phi(x,0) = \phi(x,1)$ and $v(x,0) = -v(x,1)$. For the side boundaries, transmissive (or free inflow/outflow) boundaries were used. This was implemented using ghost cells such that $\phi(0,y) = \phi(1,y)$ and $u(0,y) = u(1,y)$ on the left boundary, and $\phi(n+1,y) = \phi(n,y)$ and $u(n+1,y) = u(n,y)$, assuming n number of cells in the x direction. The upper boundary height (between the dense underflow and ash cloud) and the depth-averaged solids concentration were updated in each time step through the experimentally determined values of H_U and $\tilde{\phi}$. To ensure convergence, we also tested that the Courant–Friedrichs–Lewy condition was satisfied at each time step.

DEM modelling. Computational fluid dynamics (CFD) numerical simulations were performed using a modified version of the MFIX numerical open-source code developed and supported by the US Department of Energy and National Energy Technology Laboratory. We adopted the Lagrangian–Eulerian approach to model particle–particle and hydrodynamic interactions with four-way coupling[31]. The soft-sphere approach, which uses the spring–dashpot system, allowed us to model collisions, frictional contacts, fluid drag, buoyancy and coupling between phases through momentum exchange. More details regarding the physics used in MFIX can be found in the open documentation regarding the multiphase code. Simulations were run on the ATLAS cluster of the Georgia Institute of Technology.

The DEM of MFIX has been already validated comprehensively, as well as the DEM coupling with a Eulerian phase. Nonetheless, we decided to test the validity of the 2.5-dimension (edge effects in the z direction are ignored; y = vertical; and x = horizontal) simulation against three-dimensional experiments, to ensure that gas–solid coupling was well described for our application. Therefore, we ran numerical simulations of defluidization. There, we set an initial 'hydrostatic' (linear) pressure profile of the interstitial air within a packed bed of glass beads of 200 μm diameter and compared the estimated vertical gas velocity and defluidization time with measurements of equivalent parameters in experiments designed specifically for this study. We obtained a match between experimental and numerical results within 95%.

To investigate the effect of shear on the pore fluid pressure in a gas-particle system, a computational domain of 0.2 m in height, 0.01 m in width and a depth equivalent to the particle diameter (66×10^{-6} m) was created. The solid phase was composed of monodisperse spheres of equivalent diameter equal to the product of the Sauter mean diameter and sphericity of our experimental mixture (66 μm). This value was validated by performing fluidization experiments, which allowed us to estimate the equivalent diameter of our polydisperse mixture as 65 ± 2 μm. Using

the equivalent diameter ensures that the drag force of the fluid on the solid phase was described accurately.

In total, 6.7×10^5 particles to which we attributed the mean density of the experimental mixture ($1,950\,kg\,m^{-3}$) were simulated. Frictional properties of the particle–particle (static friction coefficient of particles = 0.8) and particle–wall interactions (particle–wall friction coefficient = 0.7) were derived from the experimental mixture (restitution coefficient = 0.5). The values used for the particle stiffness coefficient (k_n and k_t) are lower than those of natural pyroclastic rocks, allowing us to run simulations within practical time limits and, as we have tested, ensure random close packing of spheres matching theoretical estimates (particle volumetric concentration = 64 volume %).

The fluid was set as air, with a molecular weight of $28.97\,g\,mol^{-1}$. The air pressure was imposed by defining a pressure at the upper domain boundary, and the air density was solved using the equation of state of ideal gas law. The air temperature was chosen as 400 °C for an equivalent dynamic viscosity of $3.3 \times 10^{-5}\,Pa\,s^{-1}$.

To reduce the computational demand, we imposed vertical periodic boundary conditions, while the upper boundary condition was set as 'pressure outflow' and a constant gas pressure of $1.01 \times 10^5\,Pa$. The lower boundary condition was smooth and set as 'no-slip' for the fluid, whereas it was set as a wall-friction boundary for the particles. The time step was adaptive and restrained to a value below 0.5×10^{-4}, thus ensuring that particles travelled across the domain in several time steps before entering the periodic boundaries. The grid size was defined as $7.9 \times 10^{-4}\,m$ in the vertical direction and $1 \times 10^{-3}\,m$ in the horizontal direction. Simulations at higher resolutions (up to $2 \times 10^{-4}\,m$) showed similar results to the simulations enunciated

above, thus we chose the coarsest grid that showed reproducibility to minimize computational duration.

The study focused solely on the effect of shear in the lower base of a gas-particle mixture. As the DEM-CFD simulation of greater than decimetre thicknesses is not practical (too many particles are required), using a pressure outflow boundary condition, we varied the gas pore pressure from 250–1,000,000 Pa to simulate the various degrees of bed support of a pyroclastic flow as thick as ~100 m, if fully supported. Initially, a linear hydrostatic pore fluid pressure profile was defined, then shear was imposed on particles through a velocity profile. Solving mass and momentum conservation equations illuminated various regimes of pressure gradient (diverging from linear) for a wide range of shear gradients (up to $14 \times 10^5\,s^{-1}\,m^{-1}$) and pore pressures ($0.00025$ to $1 \times 10^6\,Pa$). A vertical velocity profile was defined from a targeted shear gradient. Each particle inside the computational domain was given a horizontal velocity based on its height. Note that the results shown in Fig. 5 were exported at the time step $t = 1\,ms$.

Data availability
The data that support the findings of this study are available from the corresponding author upon request.

Code availability
The code used to produce the DEM-CFD is freely available at https://mfix.netl.doe.gov/.